5762 *Chem. Mater.* **2010,** *22,* 5762–5773
DOI:10.1021/cm102126a

CHEMISTRY OF MATERIALS
Article

Small-Molecule Thiophene-C_{60} Dyads As Compatibilizers in Inverted Polymer Solar Cells

Jong Bok Kim,[†] Kathryn Allen,[‡] Soong Ju Oh,[§] Stephanie Lee,[†] Michael F. Toney,[∥] Youn Sang Kim,[#] Cherie R. Kagan,[§] Colin Nuckolls,[‡] and Yueh-Lin Loo*[,†]

[†]*Department of Chemical and Biological Engineering, Princeton University, Princeton, New Jersey 08544,* [‡]*Department of Chemistry, Columbia University, New York, New York 10027,* [§]*Departments of Electrical and Systems Engineering, Materials Science and Engineering, Chemistry, University of Pennsylvania, Philadelphia, Pennsylvania 19104,* [∥]*Stanford Synchrotron Radiation Lightsource, SLAC National Accelerator Laboratory, Menlo Park, California 94025, and* [#]*Department of Nano Science and Technology, Graduate School of Convergence Science and Technology, Seoul National University, Seoul 151-742, Korea*

Received July 29, 2010. Revised Manuscript Received September 2, 2010

This study details the synthesis and characterization of thiophene-C_{60} derivatives, nT-C_{60}, as compatibilizers for inverted bulk-heterojunction organic solar cells comprising poly(3-hexylthiophene), P3HT, and [6,6]-phenyl-C_{61}-butyric acid methyl ester, PCBM. We find that the extent with which these compatibilizers can reduce interfacial energy and prevent domain coarsening and macrophase separation in active layers depends strongly on their molecular architecture. 4T-C_{60} is the most effective among the derivatives tested; its incorporation at 5 wt % to P3HT and PCBM effectively suppresses macrophase separation, even upon extended thermal annealing of the active layers. In sharp contrast to 4T-C_{60}, 8T-C_{60} is miscible with P3HT. The addition of 8T-C_{60} to active layers of inverted solar cells therefore does not arrest macrophase separation on extended annealing. 2T-C_{60} is also ineffective as a compatibilizing agent, presumably because its thiophene segment is too short so its presence at the interface between P3HT and PCBM does not increase interfacial adhesion.

1. Introduction

Organic solar cells have attracted a lot of interest from the scientific community as alternatives to inorganic photovoltaics because of their potentially more straightforward fabrication and lower costs.[1−3] The operation of organic solar cells, however, differs from those of inorganic photovoltaics. Because of the low dielectric constant of the organic photoactive layer, excitons that are generated upon photoabsorption do not immediately dissociate into free carriers (as is the case with inorganic photovoltaics).[4] Energy conversion with organic solar cells thus involves several cascading events.[4,5] Starting with light absorption in the photoactive layer, the excitons that are generated must diffuse to and dissociate at the electron donor-electron acceptor interface to produce free carriers. Transport of holes and electrons through the electron donor and electron acceptor domains, respectively, leads to charge collection at the electrodes. Given that exciton diffusion lengths for organics are typically around 10 nm,[6−8] the ideal photoactive layer in organic solar cells consists of nanoscale, bicontinuous electron donor and electron acceptor phases to maximize exciton dissociation and, ultimately, charge collection. Indeed, polymer solar cells that have exhibited record efficiencies[9,10] have all comprised bulk-heterojunction type photoactive layers formed by spin coating a solution of both the electron donor and the electron acceptor; the extent of phase separation between the constituents in the solid state thus dictates the amount of interface available for exciton dissociation.

Several groups have demonstrated the ability to tune the extent of phase separation, thereby tuning the amount of interface in the photoactive layers of bulk-heterojunction polymer solar cells by depositing the organic semiconductors from solvents having different boiling temperatures and polarities,[11,12] and also by varying the subsequent

*Corresponding author. Tel: (609) 258-9091. Fax: (609) 258-0211. E-mail: lloo@princeton.edu.

(1) Brabec, C. J.; Durrant, J. R. *MRS Bull.* **2008**, *33*, 670.
(2) Coakley, K. M.; McGehee, M. D. *Chem. Mater.* **2004**, *16*, 4533.
(3) Kippelen, B.; Bredas, J. -L. *Energy Environ. Sci.* **2009**, *2*, 251.
(4) Blom, P. W. M.; Mihailetchi, V. D.; Koster, L. J. A.; Markov, D. E. *Adv. Mater.* **2007**, *19*, 1551.
(5) Forrest, S. R. *MRS Bull.* **2005**, *30*, 28.
(6) Haugeneder, A.; Neges, M.; Kallinger, C.; Spirkl, W.; Lemmer, U.; Feldmann, J.; Scherf, U.; Harth, E.; Gügel, A.; Müllen, K. *Phys. Rev. B* **1999**, *59*, 15346.
(7) Theander, M.; Yartsev, A.; Zigmantas, D.; Sundström, V.; Mammo, W.; Andersson, M. R.; Inganäs, O. *Phys. Rev. B* **2000**, *61*, 12957.
(8) Stübinger, T.; Brütting, W. *J. Appl. Phys.* **2001**, *90*, 3632.
(9) Park, S. H.; Roy, A.; Beaupre, S.; Cho, S.; Coates, N.; Moon, J. S.; Moses, D.; Leclerc, M.; Lee, K.; Heeger, A. J. *Nat. Photonics* **2009**, *3*, 297.
(10) Liang, Y.; Xu, Z.; Xia, J.; Tsai, S. -T.; Wu, Y.; Li, G.; Ray, C.; Yu, L. *Adv. Mater.* **2010**, *22*, E135.
(11) Hoppe, H.; Niggemann, M.; Winder, C.; Kraut, J.; Hiesgen, R.; Hinsch, A.; Meissner, D.; Sariciftci, N. S. *Adv. Funct. Mater.* **2004**, *14*, 1005.
(12) Liu, J.; Shi, Y.; Yang, Y. *Adv. Funct. Mater.* **2001**, *11*, 420.

Published on Web 09/27/2010

annealing conditions of the cast films.[13−15] The incorporation of volatile additives, such as octane dithiol and diiodooctane, can alter the solvent quality and allow for additional structural rearrangement to take place prior to vitrification of two-component polymer semiconductor thin films.[16,17] Chemical patterning of substrates onto which the photoactive layers are deposited can further induce phase separation in the active layers of polymer solar cells.[18−20]

As seen from the examples above, the manipulation of processing variables can provide some control over the phase separation in the photoactive layers of organic solar cells. In many of these cases, however, it is the vitrification of the photoactive layer upon cooling or upon solvent removal that arrests the phase-separated morphology. Because these structures are kinetically trapped, further coarsening of the phase-separated domains is inevitable as heat is generated during continued device operation.[14,15] This coarsening in turn reduces the density of the heterojunction interface available for exciton dissociation; devices under extended operation thus exhibit characteristics that deteriorate with time.

To prevent structural rearrangement during device operation, block copolymers comprising electron donor and electron acceptor segments have been employed as photoactive layers in organic solar cells.[21−25] Since these materials should spontaneously microphase separate to form nanoscale domains whose length scales are commensurate with the exciton diffusion length and the nanoscale domains are thermodynamically stable, block copolymers were originally touted as the ideal candidates for organic solar cells. Block copolymers containing rigid-rod, π-conjugated segments, however, do not microphase separate like conventional random-coil block copolymers; the structural development in the solid state of these materials are typically driven by crystallization of the rigid-rod segment.[26] The device characteristics of organic solar cells with photoactive layers comprising block copolymers have thus been disappointingly low.[22,23]

To alter the thermodynamics of phase separation in polymer blends comprising P3HT and PCBM, we recently incorporated fractional amounts of nonvolatile additives in the photoactive layers of organic solar cells.[27] These additives, hydrophobic in nature, selectively partition into the P3HT domains. This preferential segregation in turn alters the extent of chemical incompatibility between phase-separated domains, providing some level of thermodynamic control over the morphological development of photoactive layers. Borrowing from established methods of blending two or more chemically incompatible polymers, compatibilizers have also been introduced in an attempt to stabilize the interfaces between domains of electron donors and acceptors in the photoactive layers of organic solar cells.[28−31] Also known as interfacial agents, these materials generally reside at the interface between the electron donor and acceptor to minimize unfavorable enthalpic contacts. Their presence at the interface thus prevents coarsening of the phase-separated domains upon thermal annealing. Devices comprising compatibilized polymer blends should thus exhibit characteristics that are robust and stable because their photoactive layers are resistant to subsequent structural changes on extended operation.

Block copolymers have been incorporated in fractional quantities as potential compatibilizers for organic semiconductor constituents. Rajaram et al,[28] and Yang et al.,[29] for example, reported the incorporation of 5−25 wt % P3HT-containing block copolymers within the active layers of P3HT and PCBM bulk-heterojunction organic solar cells. While these devices exhibit an apparent increase in short-circuit current densities compared with reference devices, the performance of these devices were not tracked with extended thermal annealing so the efficacy of the block copolymers as compatibilizers was not demonstrated. More recent studies by Sivula et al.[30] and Lee et al.[31] based on slight variants of the block copolymers previously studied demonstrated suppression of macrophase separation in active layers comprising P3HT and PCBM on thermal annealing. As a consequence, the characteristics of these latter devices are stable and robust with extended annealing. The short-circuit current densities of these devices, however, are lower than those initially exhibited by the uncompatibilized, reference devices. This reduction in short-circuit current density was attributed to the presence of large insulating groups or saturated hydrocarbon backbones in these block copolymers that ultimately hinder charge separation and transport at the electron donor−electron acceptor interface.[30]

Instead of high-molecular-weight block copolymers, we have chosen to evaluate solution-processable small-molecule donor−acceptor dyads with minimal insulating

(13) Li, G.; Shrotriya, V.; Yao, Y.; Yang, Y. *J. Appl. Phys.* **2005**, *98*, 043704.
(14) Peumans, P.; Uchida, S.; Forrest, S. R. *Nature* **2003**, *425*, 158.
(15) Zhong, H.; Yang, X.; deWith, B.; Loos, J. *Macromolecules* **2006**, *39*, 218.
(16) Lee, J. K.; Ma, W. L.; Brabec, C. J.; Yuen, J.; Moon, J. S.; Kim, J. Y.; Lee, K.; Bazan, G. C.; Heeger, A. J. *J. Am. Chem. Soc.* **2008**, *130*, 3619.
(17) Yao, Y.; Hou, J.; Xu, Z.; Li, G.; Yang, Y. *Adv. Funct. Mater.* **2008**, *18*, 1783.
(18) Chen, F. -C.; Lin, Y. -K; Ko, C. -J. *Appl. Phys. Lett.* **2008**, *92*, 023307.
(19) Park, L. Y.; Munro, A. M.; Ginger, D. S. *J. Am. Chem. Soc.* **2008**, *130*, 15916.
(20) Wei, J. H.; Coffey, D. C.; Ginger, D. S. *J.Phys. Chem. B* **2006**, *110*, 24324.
(21) Lee, S. S.; Loo, Y. -L. *Annu. Rev. Chem. Biomol. Eng.* **2010**, *1*, 59.
(22) Tao, Y.; McCulloch, B.; Kim, S.; Segalman, R. A. *Soft Matter* **2009**, *5*, 4219.
(23) Zhang, Q.; Cirpan, A.; Russell, T. P.; Emrick, T. *Macromolecules* **2009**, *42*, 1079.
(24) Sommer, M.; Huettner, S.; Thelakkat, M. *Adv. Polym. Sci.* **2010**, *228*, 123.
(25) Roncali, J. *Chem. Soc. Rev.* **2005**, *34*, 483.
(26) Iovu, M. C.; Jeffries-El, M.; Zhang, R.; Kowalewski, T.; McCullough, R. D. *J. Macromol. Sci. A* **2006**, *43*, 1991.
(27) Kim, C. S.; Tinker, L. L.; DiSalle, B. F.; Gomez, E. D.; Lee, S.; Bernhard, S.; Loo, Y. -L. *Adv. Mater.* **2009**, *21*, 3110.
(28) Rajaram, S.; Armstrong, P. B.; Kim, B. J.; Fréchet, J. M. J. *Chem. Mater.* **2009**, *21*, 1775.
(29) Yang, C.; Lee, J. K.; Heeger, A. J.; Wudl, F. *J. Mater. Chem.* **2009**, *19*, 5416.
(30) Sivula, K.; Ball, Z. T.; Watanabe, N.; Fréchet, J. M. J. *Adv. Mater.* **2006**, *18*, 206.
(31) Lee, J. U.; Jung, J. W.; Emrick, T.; Russell, T. P.; Jo, W. H. *J. Mater. Chem.* **2010**, *20*, 3287.

Scheme 1. Chemical Structures of 2T-C_{60}, 4T-C_{60} and 8T-C_{60}

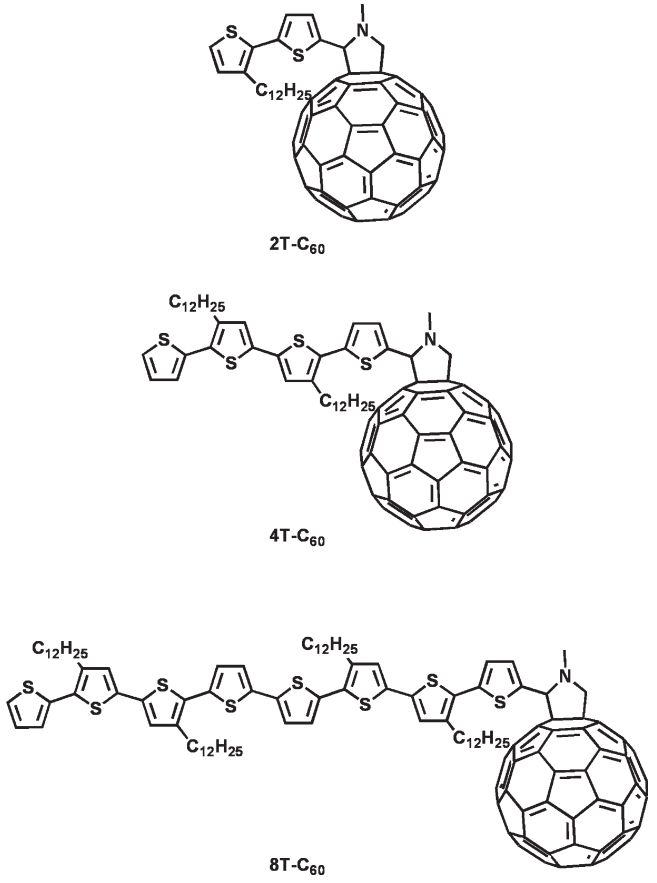

linker in between the electrically active moieties as potential compatibilizers for P3HT and PCBM. In this study, the thiophene-C_{60} dyads are designated nT-C_{60}, where n represents the number of thiophene units attached to the fullerene. Scheme 1 shows the chemical structures of the dyads explored in this study. These derivatives were synthesized directly from the corresponding thiophene-carbaldehyde via the well-known Prato reaction.[32] The similarities in the chemical structures of nT-C_{60} to P3HT and PCBM should encourage their placement at the electron donor-electron acceptor interface. Similar dyads have been reported as electron transfer agents;[33−35] their incorporation into the active layers of P3HT:PCBM polymer solar cells should thus not compromise the electronic properties of the resulting devices as a consequence of compatibilization. Organic solar cells having P3HT and PCBM bulk-heterojunction photoactive layers that are compatibilized with fractional amounts of nT-C_{60} exhibit excellent device characteristics that are stable and robust, even with extended annealing. Given that minimal insulating linkers are present between the electron-donating and electron-accepting moieities of the nT-C_{60} dyads, their incorporation into the active layers of P3HT:PCBM solar cells does not hinder charge transport or lower short-circuit current densities. We find that the architecture of the interfacial agent strongly influences its ability to compatibilize; 4T-C_{60} is the most effective compatibilizer among those we tested.

2. Experimental Section

2−1. Synthesis of nT-C_{60} Dyads. *General Procedures*. Unless otherwise noted, all reagents were used as-received and all reactions were carried out under a nitrogen atmosphere. Column chromatography was carried out using normal phase silica gel. When specified, column chromatography was performed on a CombiFlash Rf system with Redisep normal phase silica columns (Teledyne ISCO Inc., Lincoln, NE). ^{1}H NMR and ^{13}C NMR spectra were measured in deuterated chloroform with 0.03% v/v TMS and recorded on Bruker DRX-300 or Bruker DRX-400 spectrometers at room temperature. High-resolution mass spectra were recorded on a JEOL JMSHX110A/110A tandem mass spectrometer. Matrix assisted laser desorption ionization (MALDI) mass spectra were taken on Voyager-DE AB Applied Biosystems (Framingham MA, USA) using an accelerating potential of 20 kV, a UV laser of 337 nm and with dithranol as a matrix. 3-Dodecylthiophene (**2**) and 2-bromo-3-dodecylthiophene (**3**) were synthesized and characterized using known literature procedures from commercially available 3-bromothiophene (**1**).[36]

Tributyl(3-dodecylthiophene-2-yl)stannane (***4***). n-Butyllithium (1.6 M, 10.4 mL, 16.6 mmol) was added slowly dropwise to a 3-neck flask, which contained a solution of **3** (5.0 g, 15.2 mmol) in 50 mL of dry THF at −78 °C. Lithiation was monitored by thin layer chromatography (TLC) against 3-dodecylthiophene in hexanes. After lithiation was completed (∼1 h), tributyl stannyl-chloride (4.9 mL, 18.2 mmol) was added and the reaction was slowly warmed to room temperature and left for 6 h. Unreacted dodecylthiophene was distilled off and the remainder was used without further purification. ^{1}H NMR (300 MHz, $CDCl_3$): δ (ppm) = 7.53 (d, J = 4.6 Hz, 1H), 7.10 (d, J = 4.6 Hz, 1H), 2.59 (t, J = 8.1 Hz, 2H), 1.65−0.87 (m, 50 H).

3′-Dodecyl-2,2′-bithiophene-5-carbaldehyde (***5***). Compound **5** was prepared via Stille coupling[37] between **4** and commercially available 5-bromothiophene-2-carbaldehyde. The crude material was purified using the CombiFlash ISCO (30% dichloromethane/hexanes) and the resulting brown solid was isolated in 53% yield (296.6 mg, 0.8189 mmol). ^{1}H NMR (300 MHz, $CDCl_3$): δ (ppm) = 9.88 (s, 1H), 7.70 (d, J = 3.9 Hz, 1H), 7.28 (d, J = 5.1 Hz, 1H), 7.21 (d, J = 3.9 Hz, 1H), 6.97 (d, J = 5.1 Hz, 1H), 2.81 (t, J = 7.8 Hz, 2H), 1.65 (m, 2H), 1.30 (m, 18H), 0.88 (t, J = 7.1 Hz, 3H); ^{13}C NMR δ (ppm) 182.8, 146.8, 142.5, 142.2, 136.8, 130.8, 129.7, 126.4, 125.9, 32.1, 30.6, 29.8, 29.7 (multiple peaks), 29.6, 29.5, 22.8, 14.2; FAB+ Calcd: $C_{21}H_{30}OS_2$ (363.1816). Obsd: 363.1817.

5,5′-Dibromo-4,4′-didodecyl-2,2′-bithiophene (***6***). Compound **6** was synthesized via homocoupling[37] of **3**. The solid was purified by column chromatography (100% hexanes). The dark yellow solid was isolated in 77% yield (17.58 g, 26.61 mmol). ^{1}H NMR (400 MHz, $CDCl_3$): δ (ppm) = 6.77 (s, 2H), 2.52 (t, J = 7.8 Hz, 4H), 1.57 (m, 4H), 1.31−1.26 (m, 36H), 0.88 (t, J = 6.8 Hz, 6H); ^{13}C NMR δ (ppm) 143.1, 136.3, 124.6, 108.0, 32.1, 29.8, 29.7 (multiple peaks), 29.5, 29.3, 22.8, 14.3.

(32) Maggini, M.; Scorrano, G. *J. Am. Chem. Soc*. **1993**, *115*, 9798.
(33) Fujitsuka, M.; Masuhara, A.; Kasai, H.; Oikawa, H.; Nakanishi, H.; Ito, O.; Yamashiro, T.; Aso, Y.; Otsubo, T. *J. Phys. Chem. B* **2001**, *105*, 9930.
(34) Narutaki, M.; Takimiya, K.; Otsubo, T.; Harima, Y.; Zhang, H.; Araki, Y.; Ito, O. *J. Org. Chem*. **2006**, *71*, 1761.
(35) Negishi, N.; Takimiya, K.; Otsubo, T.; Harima, Y.; Aso, Y. *Synth. Met*. **2005**, *152*, 125.
(36) Bäuerle, P.; Pfau, F.; Schlupp, H.; Würthner, F.; Gaudl, K. -U.; Caro, M. B.; Fischer, P. *J. Chem. Soc., Perkin Trans. 2*. **1993**, 489.
(37) Takahashi, M.; Masui, K.; Sekiguchi, H.; Kobayashi, N.; Mori, A.; Funahashi, M.; Tamaoki, N. *J. Am. Chem. Soc*. **2006**, *128*, 10930.

3′,4″-Didodecyl-2,2′:5′,2″:5″,2‴:5‴,2⁗-quaterthiophene (*7*). Compound **7** was prepared via a Stille coupling[37] between **6** and 2.5 equiv. of commercially-available tributyl(thiophen-2-yl)-stannane. The modified workup is as follows. The crude residue was taken up in a saturated KF/THF/water bath for 24 h. The organic layer was extracted with dichloromethane and washed with saturated NH_4Cl and then water. The organic layer was dried and concentrated in vacuo and purified by column chromatography (100% hexanes). The resulting brown solid was recrystallized from ethanol to yield a yellow solid in 81% yield. ^{1}H NMR (400 MHz, $CDCl_3$): δ (ppm) =7.30 (dd, J = 5.0, 1.0 Hz, 2H), 7.13 (dd, J = 3.6, 1.0 Hz, 2H), 7.07 (dd, J = 5.0, 3.6 2H), 6.99 (s, 2H), 2.73 (t, J = 8.0 Hz, 4H), 1.65 (m, 4H), 1.38−1.26 (m, 36H), 0.88 (t, J = 6.4 Hz, 6H); ^{13}C NMR δ (ppm) 140.5, 136.1, 135.0, 129.7, 127.6, 126.5, 125.9, 125.4, 32.1, 30.7, 29.8, 29.7 (x2), 29.6 (multiple peaks), 29.5, 22.8, 14.3.

3′,4″-Didodecyl-2,2′:5′,2″:5″,2‴:5‴,2⁗-quaterthiophene-5-carbaldehyde (*8*). In a dry, 3-neck flask fitted with a condenser, $POCl_3$ (0.14 mL, 1.53 mmol) and DMF (0.16 mL, 2.07 mmol) were added to 15 mL of dichloroethane at 0 °C. A solution of **7** (1.00 g, 1.50 mmol) in 26 mL of dichloroethane was added slowly dropwise. The reaction was heated to reflux for four days and then cooled and quenched with 1 M HCl at 0 °C. After extraction with dichloromethane, the organic layer was washed 3× with water, dried over anhydrous $MgSO_4$, filtered, and concentrated in vacuo. The yellow-brown solid was purified using the CombiFlash ISCO system (100% hexanes to 75% dichloromethane/hexanes) to give an orange solid in 49% yield (515.70 mg, 0.74 mmol). ^{1}H NMR (300 MHz, $CDCl_3$): δ (ppm) = 9.88 (s, 1H), 7.70 (d, J = 4.0 Hz, 1H), 7.32 (dd, J = 5.1, 1.2 Hz, 1H), 7.21 (d, J = 4.0 Hz, 1H), 7.14 (dd, J = 3.6, 1.2 Hz, 1H), 7.07 (dd, J = 5.1, 3.6 Hz, 1H), 7.04 (s, 1H), 7.02 (s, 1H), 2.82−2.71 (m, 4H), 1.74−1.61 (m, 4H), 1.43−1.26 (m, 36H), 0.88 (t, J = 6.6 Hz, 6H); ^{13}C NMR δ (ppm) 182.6, 146.3, 143.2, 142.2, 140.7, 137.3, 136.9, 135.8, 134.2, 130.7, 128.5, 127.6, 127.3, 127.0, 126.1, 125.9, 125.7, 32.0, 30.7, 30.3, 30.0, 29.8, 29.7 (multiple peaks), 29.6, 29.5, 22.8, 14.2; FAB+ Calcd: $C_{41}H_{58}OS_4$ (694.3371). Obsd: 694.3381.

5‴-Bromo-3′,4″-didodecyl-2,2′:5′,2″:5″,2‴:5‴,2⁗-quaterthiophene-5-carbaldehyde (*9*). In a 150 mL round-bottom flask, **8** (633 mg, 0.911 mmol) was brominated in 60 mL of acetic acid with freshly recrystallized *N*-bromosuccinimide (162 mg, 0.911 mmol) at room temperature. The mixture was allowed to stir overnight. The reaction was quenched by addition of water and the organic material was extracted with dichloromethane, dried over anhydrous $MgSO_4$, filtered, and concentrated in vacuo. The residue was taken up in cold hexanes/ether and filtered to remove succinimide. The orange solid was recovered without further purification in 97% yield. (682 mg, 0.881 mmol) ^{1}H NMR (400 MHz, $CDCl_3$): δ (ppm) = 9.88 (s, 1H), 7.71 (d, J = 3.9 Hz, 1H), 7.22 (d, J = 3.9 Hz, 1H), 7.03 (m, 3H), 6.88 (d, J = 3.9 Hz, 1H), 2.79 (t, J = 7.8 Hz, 2H), 2.68 (t, J = 7.8 Hz, 2H), 1.74−1.59 (m, 4H), 1.45−1.23 (m, 36H), 0.88 (m, 6H); ^{13}C NMR δ (ppm) 182.6, 146.2, 143.2, 142.4, 141.2, 137.3, 137.0, 136.9, 134.8, 130.5, 129.6, 128.7, 127.2, 126.4, 126.0, 112.3, 32.1, 30.7, 30.4, 30.0, 29.8, 29.7 (multiple peaks), 29.6, 29.5, 22.8, 14.3; FAB+ Calcd: $C_{41}H_{57}OBrS_4$ (772.2476). Obsd: 772.2474.

5-Bromo-3′,4″-didodecyl-2,2′:5′,2″:5″,2‴:5‴,2⁗-quaterthiophene (*11*). In a dry, 250 mL 3-neck flask, **7** (2.00 g, 3.00 mmol) was dissolved in 175 mL of THF and cooled to 0 °C. In the dark, freshly recrystallized *N*-bromosuccinimide (534 mg, 3.00 mmol) was added neat in two equal portions over 1 h. The reaction was slowly warmed to room temperature after addition. The reaction was left in the dark for 6 h, and water was then added and the organic material was extracted with dichloromethane. The product was purified with column chromatography (100% hexanes). The yellow solid was recovered in 39% yield (865 mg, 1.16 mmol). ^{1}H NMR (400 MHz, $CDCl_3$): δ (ppm) = 7.31 (dd, J = 5.1, 0.9 Hz, 1H), 7.13 (dd, J = 3.6, 0.9 Hz, 1H), 7.07 (dd, J = 5.1, 3.6 Hz, 1H), 7.01 (d, J = 4.0 Hz, 1H), 6.99 (s, 1H), 6.97 (s, 1H), 6.86 (d, J = 4.0 Hz, 1H), 2.74−2.66 (m, 4H), 1.64 (m, 4H), 1.38−1.26 (m, 36H), 0.88 (t, 6.0 Hz, 6H); ^{13}C NMR δ (ppm) 141.0, 140.5, 137.6, 136.0, 135.6, 134.7, 130.4, 130.0, 128.6, 127.6, 126.7, 126.4, 126.1, 126.0, 125.5, 112.0, 32.1, 30.7, 29.8, 29.7 (multiple peaks), 29.6, 29.5, 22.8, 14.3.

Tributyl(3′,4″-didodecyl-2,2′:5′,2″:5″,2‴:5‴,2⁗-quaterthiophen-5-yl)-stannane (*12*). In a dry 50 mL flask, **11** (500 mg, 0.670 mmol) was dissolved in 12 mL of THF and cooled to 0 °C. n-Butyllithium (1.6 M, 0.419 mL, 0.670 mmol) was dripped in slowly and when the lithiation was complete as indicated by TLC, (∼2 h) tributyltin chloride (0.217 mL, 0.804 mmol) was added. The reaction was warmed to room temperature and allowed to stir overnight. The organic material was extracted with dichloromethane and washed 3× with water. The organic layer was dried over anhydrous $MgSO_4$, filtered, and concentrated in vacuo. The material was used without further purification. ^{1}H NMR (400 MHz, $CDCl_3$): δ (ppm) = 7.30 (m, 1H), 7.24 (m, 1H), 7.12 (m, 2H), 7.07 (m, 1H), 6.98 (m, 2H), 2.73 (m, 4H), 1.64−0.88 (m, 73H).

3′,4″,3⁗′,4⁗′-Quaterdodecyl-2,2′:5′,2″:5″,2‴:5‴,2⁗:5⁗′,2⁗′:5⁗′,2⁗′:5′⁗′,2″⁗′:5″⁗′,2‴⁗′:5‴⁗′,2⁗′⁗′:5⁗′⁗′,2⁗′⁗′-octithiophene-5-carbaldehyde (*10*). In a dry, 100 mL 3-neck flask fitted with a condenser, **9** (682 mg, 0.881 mmol) was dissolved in 40 mL of toluene and $Pd(PPh_3)_4$ (51 mg, 0.044 mmol) was added. **12** (842 mg, 0.881 mmol) was added via syringe. The reaction was refluxed for 2 h and another 20 mg of **12** was added. Reflux was continued for 6 more hours and when there was no more reaction as indicated by TLC, the solution was cooled and concentrated and the organic material was dissolved in dichloromethane and washed 2× with water. The organic layer was stirred in a saturated KF/THF/water solution for 12 h and then extracted, dried over anhydrous $MgSO_4$, filtered, and concentrated. The bright orange residue was purified using the CombiFlash ISCO system (5% dichloromethane/hexanes to 30% dichloromethane/hexanes) to yield a bright red solid in 37% yield (434 mg, 0.319 mmol). ^{1}H NMR (400 MHz, $CDCl_3$): δ (ppm) = 9.88 (s, 1H), 7.70 (d, 3.9 Hz, 1H), 7.31 (d, J = 5.1 Hz, 1H), 7.22 (d, J = 3.9 Hz, 1H), 7.15−7.14 (m, 3H), 7.09−7.00 (m, 7H), 2.82−2.71 (m, 8H), 1.69 (m, 8H), 1.39−1.26 (m, 72H), 0.88 (m, 12H);^{13}C NMR δ (ppm) 182.7, 146.3, 143.3, 142.3, 140.8, 140.7, 140.5 (multiple peaks), 137.2, 137.0, 136.7, 136.1, 135.4, 135.2, 134.9, 134.3, 130.5, 129.9, 129.4, 128.6, 127.6, 127.5, 127.1, 126.7 (multiple peaks), 126.4, 126.0, 125.5, 124.2, 124.1, 32.1, 30.7, 30.6, 30.4, 29.8, 29.7 (multiple peaks), 29.6, 29.5, 22.8, 14.3; FAB+ Calcd: $C_{81}H_{114}OS_8$ (1358.66). Obsd: (1359.08).

Synthesis of Thiophene−Fullerene Dyads. A typical procedure for the Prato Reaction[32] of aldehydes **5**, **8**, and **10** with C_{60} is as follows: in a dry, 2-neck flask fitted with a condenser, C_{60} (62.0 mg, 0.0861 mmol) was dissolved in 15 mL of dry chlorobenzene. Subsequently, 0.8 equiv. of aldehyde and 2.5 equiv. of sarcosine were added. The reaction was left stirring overnight at reflux and monitored by TLC in carbon disulfide. When the aldehyde was completely depleted, the solution was concentrated and purified by a carbon disulfide column. The brown solid collected was taken up in hot THF and then poured into ethanol that had been cooled to −30 °C. The resulting brown precipitate was filtered and the filter cake was dried and characterized.

2T-C_{60} Dyad. Yield: 28%. (Note: This is the only dyad in which double addition of the aldehyde was a competitive byproduct.) ^{1}H NMR (400 MHz, $CDCl_3$): δ (ppm) = 7.34

(d, J = 3.6 Hz, 1H), 7.15 (d, J = 5.2 Hz, 1H), 7.01 (d, J = 3.6 Hz, 1H), 6.89 (d, J = 5.2 Hz, 1H), 5.26 (s, 1H), 5.00 (d, J = 9.6 Hz, 1H), 4.26 (d, J = 9.6 Hz, 1H), 2.96 (s, 3H), 2.68 (m, 2H), 1.53 (m, 2H), 1.21 (m, 18H), 0.88 (t, J = 7.2 Hz, 3H). ^{13}C NMR δ 156.0, 154.1, 153.4, 153.2, 147.5, 147.4, 147.0, 146.5 (multiple peaks), 146.4, 146.4, 146.3, 146.1, 145.7, 145.5 (multiple peaks), 145.4 (×2), 144.9, 144.80, 143.33, 143.1, 142.9, 142.8, 142.3 (multiple peaks), 142.2, 142.1, 141.9, 141.8, 140.7, 140.3, 140.2, 140.08, 139.8, 137.8, 136.8, 136.1, 135.8, 130.6, 130.3, 128.5, 128.4, 125.4, 123.9, 79.7, 70.2, 68.9, 66.0, 40.6, 32.1, 30.8, 29.9, 29.6 (multiple peaks), 29.4, 22.9, 14.3. MALDI-TOF MS: $C_{83}H_{35}NS_2$ (1109.2) m/z = 1110.9 [M^+].

4T-C_{60} Dyad. Yield: 47%. ^{1}H NMR (300 MHz, $CDCl_3$): δ (ppm) = 7.37−7.31 (m, 2H), 7.13 (m, 1H), 7.09−7.05 (m, 2H), 6.98 (s, 1H), 6.95 (s, 1H), 5.23 (s, 1H), 5.00 (d, J = 9.7 Hz, 1H), 4.26 (d, J = 9.7 Hz, 1H), 2.96 (s, 3H), 2.76−2.66, (m, 4H), 1.52 (m, 4H), 1.25 (m, 36H), 0.88 (t, 6H). ^{13}C NMR δ (ppm) 156.0, 154.0, 153.4, 153.2, 147.5, 147.2, 147.0, 146.5 (multiple peaks), 146.4, 146.3, 146.3, 146.1, 146.0, 145.8, 145.7, 145.6 (multiple peaks), 145.5, 145.5, 145.4, 144.9, 144.8, 144.6, 143.3, 143.2, 142.9, 142.8, 142.4 (multiple peaks), 142.3, 142.2, 142.1, 142.1, 141.9, 141.8, 140.9, 140.8, 140.6, 140.4, 137.5, 137.2, 136.8, 136.1, 135.8, 135.2, 135.0, 129.8 (multiple peaks), 129.6, 128.6, 127.6, 126.7, 126.0 (x2), 125.5, 125.2, 79.7, 70.2, 69.0, 40.6, 32.1, 30.7, 30.6, 29.8 (multiple peaks), 29.7, 29.5, 22.9, 14.3. MALDI-TOF MS: $C_{103}H_{63}NS_4$ (1441.4) m/z = 1442.3 [M^+].

8T-C_{60} Dyad. Yield: 37%. ^{1}H NMR (300 MHz, $CDCl_3$): δ (ppm) = 7.35 (d, J = 3.9 Hz, 1H), 7.30 (dd, J = 5.1, 0.9 Hz, 1H), 7.11 (m, 3H), 7.04 (m, 4H), 6.97 (m, 4H), 5.26 (s, 1H), 5.00 (d, J = 9.5 Hz, 1H), 4.27 (d, 9.5 Hz, 1H), 2.96 (s, 3H), 2.81−2.70 (m, 8H), 1.75−1.58 (m, 8H), 1.45−1.26 (m, 72H), 0.88 (m, 12H). ^{13}C NMR δ (ppm) 155.9, 153.4, 153.2, 153.1, 147.4, 146.5, 146.4 (×2), 146.3 (multiple peaks), 146.2 (×2), 146.1, 145.9, 145.7 (x2), 145.6 (multiple peaks), 145.5 (×2), 145.4 (×3), 144.5, 143.3, 143.1, 142.8, 142.7, 142.4, 142.3, 142.2, 142.1, 142.0, 141.8, 141.7, 140.8, 140.6, 140.4, 140.3, 140.1, 137.2, 136.9, 136.8, 136.7 (multiple peaks), 136.1, 135.7, 135.3, 135.2, 135.1, 134.9, 129.9, 129.8 (multiple peaks), 129.6, 129.5, 128.7, 128.5, 127.5, 126.7, 126.6 (×2), 126.5 (multiple peaks), 126.0, 125.5, 125.2, 124.1, 79.6, 70.1, 68.8, 40.5, 32.1, 30.6, 29.9, 29.7, 29.6 (multiple peaks), 22.9, 14.3. MALDI-TOF MS: $C_{143}H_{119}NS_8$ (2105.7) m/z = 2106.4 [M^+].

2−2. Fabrication and Characterization of Organic Solar Cell Devices with nT-C_{60} dyads. *Cyclic Voltammetry Measurement*. Cyclic voltammetry was conducted to measure the energy levels of 4T-C_{60}, P3HT, and PCBM on a CHI-660 electrochemical workstation (CH-Instruments). In the case of 4T-C_{60}, we first prepared 23 wt % (0.1M) tetrabutyl ammonium hexafluorophosphate, $(nBu)_4NPF_6$, solution as the supporting electrolyte in acetonitrile. After mixing it with 0.05 wt % test solution of 4T-C_{60} dissolved in chlorobenzene, a total of 10 μL of 2.5 wt % ferrocene solution in acetonitrile was added as the internal standard to 13 mL of test solution. For P3HT and PCBM, toluene and chlorobenzene were used as solvents to prepare the respective test solutions at the same concentrations. We used glassy carbon (GC), platinum wire, and silver/silver nitrate as the working, counter and reference electrodes, respectively (all purchased from CH-Instruments). Cycling rate was 100 mV/s and each measurement was cycled 3 times. Energy levels were calculated on the basis of the onset of the oxidation peak of ferrocene.

Fabrication of Organic Solar Cell Devices. Inverted organic solar cells were fabricated and tested on prepatterned ITO on glass substrates. The prepatterned ITO substrates were first sonicated in acetone and then in isopropyl alcohol for 10 min each. A 1 wt % titanium isopropoxide ($Ti[OCH(CH_3)_2]_4$; Aldrich, 99.999%) solution in isopropyl alcohol was then spin-coated on the ITO substrates at 3000 rpm for 30 s. Hydrolysis at room temperature for 1 h and then at 170 °C for 10 min converts titanium isopropoxide to a 40 nm thick titania electron transport layer.[38,39] Then, cosolutions of P3HT, PCBM, and nT-C_{60} in chlorobenzene were prepared. Here, the mass ratio of P3HT and PCBM were kept constant to 1:1, yielding a 2.4 wt % solution; nT-C_{60} was added as-specified with respect to the total weight of P3HT and PCBM. To compare the effectiveness of nT-C_{60} as a compatibilizer, we kept the weight (or molar) ratio of nT-C_{60} to P3HT:PCBM the same at 5 wt % (or 1 mol %). The solutions were stirred overnight; they were then spin-coated on the titania-coated ITO substrates at 500 rpm for 60 s. To optimize the concentration of nT-C_{60}, P3HT:PCBM photoactive layers with different amounts of 4T-C_{60} were annealed at 170 °C for 1 min in air before testing. For the stability test, P3HT:PCBM with nT-C_{60} active layers were annealed at 170 °C for 1 min, 1 h, and 3 h in a N_2 atmosphere to prevent degradation of PCBM on extended annealing. These devices were subsequently brought out of the glovebox for testing. Evaporation of 100 nm thick gold top electrodes through a stencil mask completed electrical contact to the photoactive layers. The active area of our devices was kept constant at 0.18 cm^2. $J-V$ characteristics were acquired using a Keithley 2400 source measurement unit under AM 1.5G 100 mW/cm^2 illumination. Before device testing, all devices were illuminated for 10 min to fill the shallow electron traps in titania layer.[38] $J-V$ characteristics reported herein were obtained 5 days after device fabrication in air. During this time, oxygen doping of P3HT increases V_{oc} from 0.38 to 0.52 V.[38]

Optical Microscope (*OM*), *Scanning Electron Microscope* (*SEM*), *and Energy-Dispersive X-ray Spectroscopy* (*EDX*). A Nikon optical microscope (ME600L) was used to obtain optical micrographs in reflection mode. A SEM equipped with a field-emission gun (XL30, FEL) and a PGT-IMIX PTS EDX detector system was used to image the morphology of the polymer thin films and to perform carbon and sulfur mapping in the field of view. The acceleration voltage was kept at 5 keV to prevent beam damage to the specimens.

Grazing Incidence X-ray Diffraction (*GIXD*). GIXD experiments were performed at the Stanford Synchrotron Radiation Lightsource (SSRL) on beamline 11−3. 2D images were collected on a MAR345 image plate and the data subsequently converted into $q_{xy}-q_z$ plots. The experiments were conducted using an X-ray wavelength of 0.976 Å^{-1} and an incident angle of 0.11°. P3HT:PCBM films were prepared according to the details outlined above.

Photocurrent Mapping. Spatially-resolved photocurrent measurements were conducted by illuminating devices with the 488 nm line of an Innova 70C Spectrum Ar:Kr laser focused to a 1 μm spot size through an Olympus BX2 modified microscope. Samples were mounted on a closed-loop piezo-controlled stage (Max 301, Thor Laboratories Nanomax) allowing for low- and higher-resolution photocurrent mapping. Testing was done 5 days after device fabrication for consistency. The devices were irradiated for 1 h with a standard light source to fill the shallow electron traps in the titania layer before photocurrent mapping.[38]

(38) Kim, C. S.; Lee, S. S.; Gomez, E. D.; Kim, J. B.; Loo, Y. -L. *Appl. Phys. Lett*. **2009**, *94*, 113302.
(39) Kim, C. S.; Lee, S.; Tinker, L. L.; Bernhard, S.; Loo, Y.-L. *Chem. Mater*. **2009**, *21*, 4583.

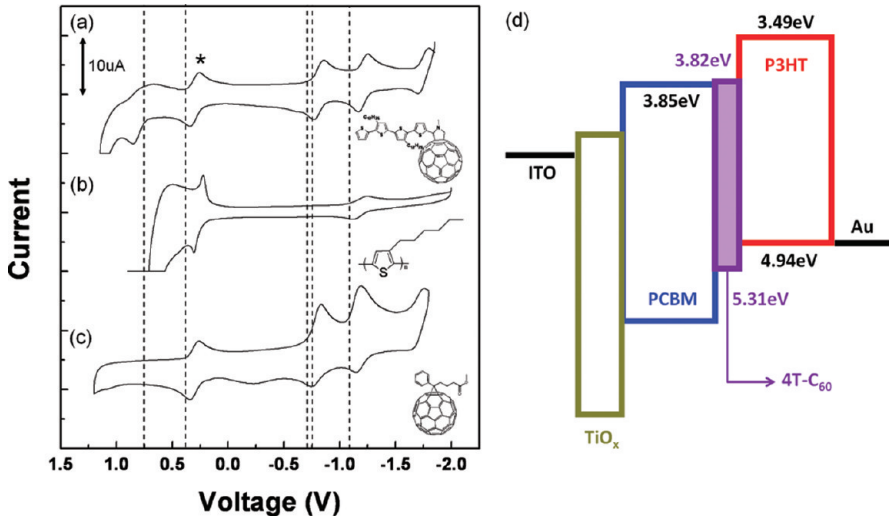

Figure 1. Cyclic voltammetry of (a) 4T-C_{60}, (b) pure P3HT, and (c) PCBM. Results indicate (d) well-matched energy levels of 4T-C_{60} with P3HT:PCBM. The chemical structures of 4T-C_{60}, P3HT, and PCBM are provided as insets.

During the photocurrent mapping experiment spanning 2.0 mm by 1.5 mm, the local photocurrent was acquired in 100 μm interval. During the higher-resolution photocurrent experiment spanning 15 μm by 15 μm, the local photocurrent data was acquired in 1 μm intervals. The photocurrent mapping experiments were completed within 30 min of initial illumination, during which we observe a negligible decrease in photocurrent generation due to the return of electron traps.

Contact Angle. Pure P3HT, PCBM and nT-C_{60} films were prepared by spin coating 1 wt % solutions of P3HT and nT-C_{60} in chlorobenzene and PCBM in chloroform on silicon wafer. Static contact angles were then measured by the sessile drop technique using deionized water and glycerol as probe liquids on an advanced goniometer (Rame-hart, USA). The surface energies were calculated using the ImagePro 300 software based on the Owens−Wendt geometric mean equation.[40]

3. Results and Discussion

We performed cyclic voltammetry to assess the redox activity of 4T-C_{60}. For comparison, we also carried out cyclic voltammetry on 0.05 wt % solutions of P3HT in toluene and PCBM in chlorobenzene. The left panel of Figure 1 contains the cyclic voltammagrams of these three species; their chemical structures are provided as insets. In each case, ferrocene was added as the internal standard. For each solution, we started at zero potential; the voltage was first swept toward reducing potentials (negative voltages) and then cycled back to oxidizing potentials (positive voltages). The redox couple with a half potential ($E_{1/2}$) of +0.29 V vs $Ag/AgNO_3$ is marked with an asterisk; it is attributed to the reduction (positive currents) and oxidation (negative currents) of ferrocene. The cyclic voltammagram in Figure 1a shows several additional redox couples at $E_{1/2}$ = −1.21, −0.81 and +0.83 V. Given the onset of the first reduction peak of 4T-C_{60} at −0.74 V, we estimated the lowest unoccupied molecular orbital (LUMO) energy level of this compound to be −3.82 eV based on the onset of the oxidation peak of ferrocene at 0.24 V and its published highest occupied molecular orbital (HOMO) energy level of −4.8 eV.[41,42] Similarly, we estimated the HOMO energy level of 4T-C_{60} based on the onset of its first oxidation peak at 0.75 V to be −5.31 eV. 4T-C_{60} thus exhibits an electrochemical band gap of 1.49 eV. For comparison, the cyclic voltammagrams of P3HT and PCBM are shown in Figures 1b and 1c, respectively. From these cyclic voltammagrams, we estimated the HOMO and LUMO energy levels of P3HT to be −4.94 and −3.49 eV, respectively. These values fall within the range of reported HOMO (between −4.84 and −5.20 eV) and LUMO (−2.89 and −3.53 eV) energy levels of P3HT in the literature.[43−46] Given the range of potential bias achievable in chlorobenzene with tetrabutyl ammonium hexafluorophosphate, we were able to observe only the redox couples associated with the reduction of PCBM; oxidation of PCBM occurred outside the experimental window. From the onset of the first reduction peak at 0.71 V, we estimated its LUMO energy level to be −3.85 eV. This value is comparable to those reported in the literature.[43,44] The energy levels estimated from cyclic voltammetry experiments are summarized in Figure 1d. 4T-C_{60} appears to have a LUMO energy level that is comparable to that of PCBM; its HOMO energy level is slightly below than that of P3HT, presumably because the extent of conjugation is significantly smaller with 4 thiophene units.[47,48]

(40) Owens, D. K.; Wendt, R. C. *J. Appl. Polym. Sci.* **1969**, *13*, 1741.
(41) He, Y.; Wu, W.; Zhao, G.; Liu, Y.; Li, Y. *Macromolecules* **2008**, *41*, 9760.
(42) Pommerehne, J.; Vestweber, H.; Guss, W.; Mahrt, R. F.; Bässler, H.; Porsch, M.; Daub, J. *Adv. Mater.* **1995**, *7*, 551.
(43) Al-Ibrahim, M.; Roth, H.-K.; Zhokhavets, U.; Gobsch, G.; Sensfuss, S. *Sol. Energy Mater. Sol. Cells* **2005**, *85*, 13.
(44) Chen, H. -Y.; Lo, M. K. F.; Yang, G.; Monbouquette, H. G.; Yang, Y. *Nat Nanotechnol.* **2008**, *3*, 543.
(45) Jiang, X.; Schaller, R. D.; Lee, S. B.; Pietryga, J. M.; Klimov, V. I.; Zakhidov, A. A. *J. Mater. Res.* **2007**, *22*, 2204.
(46) Verma, D.; Dutta, V. *J. Renewable Sustainable Energy* **2009** *1*, 023107.
(47) Peng, Q.; Park, K.; Lin, T.; Durstock, M.; Dai, L. *J.Phys. Chem. B* **2008**, *112*, 2801.
(48) Yang, G. B.; Wu, Y.; Tian, W. J.; Zhou, X.; Ren, A. M. *Curr. Appl. Phys.* **2005**, *5*, 327.

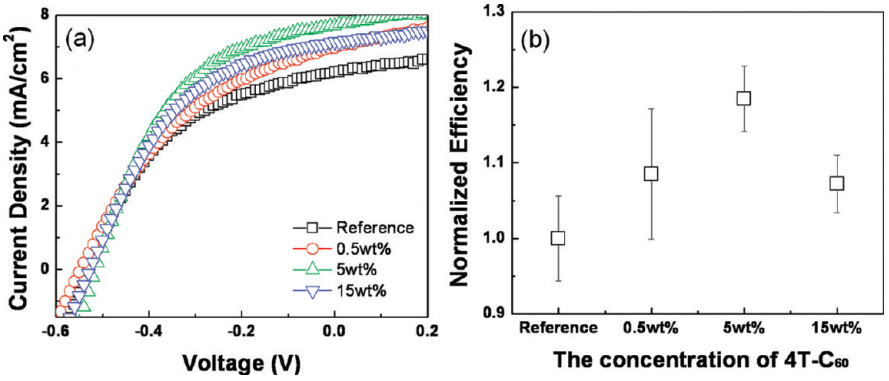

Figure 2. (a) $J-V$ characteristics and (b) normalized device efficiency of inverted P3HT:PCBM solar cells with different amounts of 4T-C_{60} in the active layers. All devices were annealed at 170 °C for 1 min in air.

Figure 2 summarizes the $J-V$ characteristics and normalized device efficiencies of inverted organic solar cells incorporating varying amounts of 4T-C_{60} in the P3HT:PCBM photoactive layer. All devices were thermally annealed at 170 °C for 1 min in air to remove residual solvent and induce crystallization of the organic semiconductor constituents. Because our devices were fabricated in the inverted architecture, we were able to assess the characteristics of the solar cells in air.[38] The inverted architecture results in power generation with positive short-circuit current densities (J_{sc}) and negative open-circuit voltages (V_{oc}).[49] The $J-V$ characteristics acquired on representative devices with varying amounts of 4T-C_{60} in the photoactive layers under illumination are shown in Figure 2a. For comparison, we have also included the $J-V$ characteristics of a reference inverted P3HT:PCBM device without any nT-C_{60} (open squares). Of five reference devices tested, the J_{sc} of P3HT:PCBM device without any nT-C_{60} (open squares) averaged 6.6 ± 0.4 mA/cm^2. Like the incorporation of P3HT-containing block copolymers,[28,29] the addition of 4T-C_{60} generally increases device J_{sc}. With the incorporation of 0.5 wt % 4T-C_{60}, the device J_{sc} increases to 7.0 ± 0.5 mA/cm^2. At 5 wt % 4T-C_{60}, the average J_{sc} from five devices tested is 7.7 ± 0.1 mA/cm^2. Further increasing the compatibilizer content, however, results in a slight decrease in device J_{sc} (6.8 ± 0.2 mA/cm^2 at 15 wt % 4T-C_{60}). On the other hand, the incorporation of 4T-C_{60} does not affect device V_{oc}; the V_{oc} of all the devices remain constant at -0.52 ± 0.01 V. Given that the energy levels of 4T-C_{60} are not significantly different from the HOMO and LUMO energy levels of P3HT and PCBM, respectively, its addition should not alter device V_{oc}. Increases in device J_{sc} stemming from the addition of 4T-C_{60} thus translate into improvements in device efficiencies, as depicted in Figure 2b. Compared with uncompatibilized, reference P3HT:PCBM polymer solar cells, the incorporation of 0.5 and 5 wt % 4T-C_{60} into the active layers increases the normalized device efficiency by 8.5 and 18.5%, respectively. Devices with 15 wt % 4T-C_{60} in the active layer exhibit a normalized average efficiency that is 7% higher than the uncompatibilized, reference devices. This observation indicates that 4T-C_{60} is an effective compatibilizer when added to P3HT and PCBM blends. Its addition effectively reduces unfavorable contacts between P3HT and PCBM, so macrophase separation is minimized. Examination of Figure 2b suggests an optimal concentration of 4T-C_{60} in the photoactive layer at which the device characteristics are maximized. This trend is also observed when diblock copolymers are used as compatibilizers for P3HT and PCBM.[29,30] That an optimal concentration exists for effective compatibilization is commonly seen in polymer−polymer blends.[50] In fact, our observations are consistent with common blends of thermoplastics, like polystyrene and polybutadiene, wherein the addition of 5−10 wt % of an interfacial agent effectively suppresses macrophase separation.[51−53] Further addition of 4T-C_{60} likely overcompatibilizes P3HT and PCBM; the resulting heterojunction interfacial density is so high that free carriers that are generated from exciton dissociation recombine before they are extracted from the interface.

To examine the effectiveness with which 4T-C_{60} compatibilizes P3HT and PCBM, we thermally annealed the photoactive layers in the presence and absence of 4T-C_{60} for extended periods; the characteristics of these inverted solar cells are shown in Figure 3. Figure 3a contains the $J-V$ characteristics of a reference P3HT:PCBM organic solar cell in which the photoactive layer was thermally annealed at 170 °C for 1 min (black open squares), 1 h (red open circles), and 3 h (green open triangles). These devices were annealed in nitrogen but tested in air to eliminate the possibility of PCBM degradation on extended annealing. In all cases, the devices exhibit a constant V_{oc} at -0.52 ± 0.01 V that is independent of thermal history. Given that the energy levels of P3HT and PCBM, and the work functions of the electrodes, should not change with thermal annealing, the V_{oc} should be the same across these devices. The device J_{sc}, on the other hand, changes significantly with thermal annealing. Of five devices that were annealed at 170 °C for 1 min, the average J_{sc}

(49) Kim, J. B.; Kim, C. S.; Kim, Y. S.; Loo, Y. -L. *Appl. Phys. Lett.* **2009**, *95*, 183301.
(50) Utracki, L. A. *Polymer Blends Handbook*; Kluwer Academic Publishers: Dordrecht, The Netherlands, 2003; Vol. *3*, Chapter 4.
(51) Chun, S. B.; Han, C. D. *Macromolecules* **2000**, *33*, 3409.
(52) Jackson, C. L.; Sung, L.; Han, C. C. *Polym. Eng. Sci.* **1997**, *37*, 1449.
(53) Thomas, S.; Prud'homme, R. E. *Polymer* **1992**, *33*, 4260.

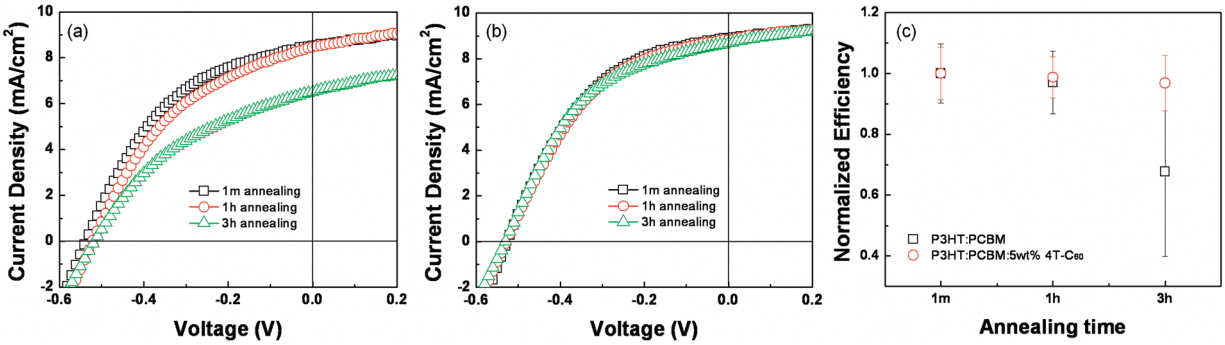

Figure 3. $J-V$ characteristics of (a) reference P3HT:PCBM devices and (b) P3HT:PCBM devices with 5 wt % 4T-C_{60} and (c) their normalized efficiencies. All devices were annealed at 170 °C under a N_2 atmosphere to prevent PCBM degradation. P3HT:PCBM devices with 4T-C_{60} maintained their efficiencies during the 3 h annealing while the reference, uncompatibilized devices exhibit decreased efficiencies after annealing.

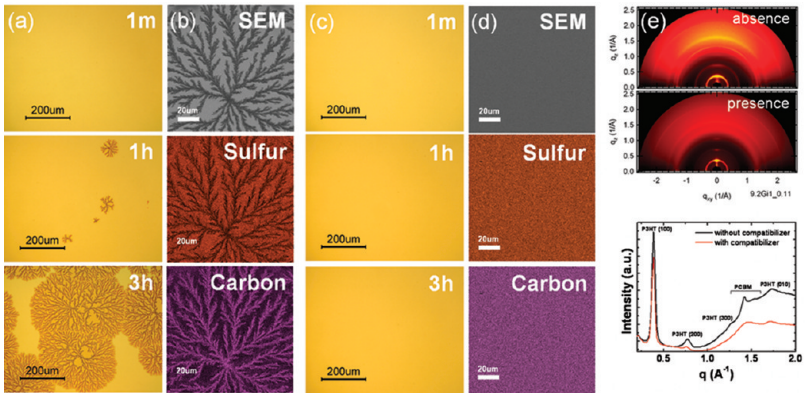

Figure 4. (a) OM and (b) SEM/EDX maps of P3HT:PCBM films annealed at 170 °C for 1 min and 1 and 3 h under a N_2 atmosphere. SEM/EDX maps were acquired from a P3HT:PCBM film annealed for 3 h, highlighting sulfur and carbon contents. (c) OM and (d) SEM/EDX maps of P3HT:PCBM films with 5 wt % 4T-C_{60} were prepared and acquired under analogous conditions. (e) 2-D GIXD images of P3HT:PCBM films (top) annealed at 170 °C for 3 h with and without 4T-C_{60} and azimuthally summed line traces of these images (bottom).

recorded was 8.47 ± 0.49 mA/cm^2. Devices that were annealed at 170 °C for 1 h exhibited comparable J_{sc}'s at 8.51 ± 0.33 mA/cm^2. Devices that were annealed for 3 h, however, showed a drop in J_{sc} (6.88 ± 1.92 mA/cm^2). These same devices also exhibited significant variability in their J_{sc}'s, as seen in the standard deviation reported above. This variability is directly correlated with the structural heterogeneities that result from macrophase separation of the active layers of the specific devices. The device whose active layer was structurally most heterogeneous exhibited the lowest J_{sc}. The $J-V$ characteristics of analogous devices in which the photoactive layers comprise 5 wt % 4T-C_{60} are shown in Figure 3b. Contrary to the reference P3HT:PCBM devices, we do not observe significant differences in the device characteristics on annealing; the average V_{oc} and J_{sc} remained at −0.53 ± 0.01 V and 8.80 ± 0.43 mA/cm^2, respectively. As such, the device efficiencies remain largely constant with extended thermal annealing. The comparison of normalized device efficiencies for these two sets of solar cells is shown in Figure 3c. The normalized device efficiencies of uncompatibilized devices drop to 67% of their original value after 3 h of thermal annealing at 170 °C. The efficiencies of devices incorporating our compatibilizer remain constant at their original value with extended annealing.

This difference in the stability of device characteristics must stem from morphological changes that result from macrophase separation on thermal annealing. To probe this structure−function relationship, we conducted structural characterization by OM, SEM in combination with EDX analysis and GIXD; the results are summarized in Figure 4. The optical micrographs in column a of Figure 4 show P3HT:PCBM thin films cast on TiOx/ITO; these films were prepared analogous to how the photoactive layers in our solar cells were prepared. The film is featureless when subjected to thermal annealing at 170 °C for 1 min. On extended annealing, however, we observe the development of dendritic structures; these dendrites span more than 50% of the thin film when P3HT:PCBM is thermally annealed at 170 °C for 3 h. The variability we observe in the J_{sc}'s of devices comprising these active layers in Figure 3a can be directly correlated with the density of dendrites in the active layer. Such structural development is characteristic of macrophase separation and domain coarsening of the constituent organic semiconductors. Although such dendritic structures have been reported on extended annealing of P3HT:PCBM blends,[54] large, faceted crystals are more commonly observed

(54) Chirvase, D.; Parisi, J.; Hummelen, J. C.; Dyakonov, V. *Nanotechnology* **2004**, *15*, 1317.

during macrophase separation of P3HT:PCBM. The structural development of P3HT:PCBM is complex and is further complicated by the fact that both constituents can crystallize. Macrophase separation is thus not only driven by the chemical incompatibility between P3HT and PCBM, it can be driven by the crystallization of one or both species. For these reasons, we attribute differences in the macrophase-separated morphology observed by different groups to differences in the thermal treatments imposed on P3HT:PCBM thin films.

To unambiguously identify the constituent that makes up the dendrites in the optical images in Figure 4a, we carried out EDX experiments, mapping specifically for sulfur and carbon content within the field of view; these results are shown in column b of Figure 4. The top panel of Figure 4b shows a SEM image of a representative dendrite structure obtained on thermal annealing P3HT:PCBM at 170 °C for 3 h. Sulfur and carbon mapping of this same region are shown below. In the sulfur map, we observe that the background is more intense compared to the dendrite. Because sulfur is an element that is unique to P3HT, this observation indicates that P3HT is preferentially enhanced in the continuous phase upon phase separation. The carbon map shown below further supports this assertion. The dendrite appears to be more carbon rich than the background. Since the number density of carbon is significantly higher in PCBM than in P3HT, we believe the dendrites that form on macrophase separation are composed of PCBM.

Column c of Figure 4 shows the optical micrographs taken on P3HT:PCBM thin films with 5 wt % 4T-C_{60}. Acquired at the same scale as Figure 4a, the micrographs appear featureless, even after the film is subjected to thermal annealing at 170 °C for 3 h. SEM and EDX mapping carried out on these films are shown in Figure 4d. Both the sulfur and carbon distributions in the thermally annealed film of P3HT:PCBM with 5 wt % 4T-C_{60} appear to be uniform, suggesting its role as an effective compatibilizer for P3HT and PCBM.

To further examine the structure of these P3HT:PCBM films, we carried out 2D GIXD. The top images of Figure 4e comprises 2D GIXD images of P3HT:PCBM films in the absence and presence of 4T-C_{60}, both annealed for 3 h at 170 °C. In the absence of 4T-C_{60}, the GIXD image acquired under nominally the same experimental conditions is significantly more intense. To quantify the structural differences between these two films, we present 1D line traces summed over all azimuthal angles for both films. Reflections associated with P3HT and PCBM are identified for clarity. In the absence of 4T-C_{60}, the GIXD line trace exhibits prominent peaks associated with the (h00) and (010) reflections of P3HT and a sharp peak at $q \approx 1.4$ Å^{-1}. This peak stems from crystalline PCBM, though its crystal structure remains undetermined.[55] In contrast, the individual reflections associated with P3HT and PCBM in the GIXD line trace of P3HT:PCBM with 4T-C_{60} are less prominent in intensity and significantly broader in peak width. In particular, we can no longer make out the crystalline peak associated with PCBM in this line trace; the broad amorphous halo around q $\sim$ 1.4 Å^{-1} suggests no significant long-range ordering of PCBM in this film. Collectively, our GIXD results show that thermal annealing P3HT:PCBM in the absence of 4T-C_{60} results in significant crystallization of both organic semiconductor constituents and suggests large-scale phase separation. The addition of 4T-C_{60} reduces macrophase separation and domain coarsening, effectively suppressing constituent crystallization in P3HT:PCBM during thermal annealing.

The deterioration in device characteristics observed in Figure 3a is thus attributed to the growth of PCBM domains on thermal annealing. The extensive coarsening of PCBM domains reduces the interfacial density between electron donor and electron acceptor, effectively decreasing exciton dissociation, and ultimately lowering J_{sc} and device efficiency. The addition of 4T-C_{60} arrests the initial structuring of P3HT:PCBM; its presence maintains the high density of heterojunction interface for efficient exciton dissociation.

To complement our structural and electrical characterization, we conducted local photocurrent measurements on our inverted polymer solar cells comprising P3HT:PCBM photoactive layers in the presence and absence of 5 wt % 4T-C_{60} after they had been annealed at 170 °C for 3 h. The devices were mounted on a piezo-driven stage and scanned with respect to 488 nm excitation focused to a 1 μm spot size. The local photocurrent was measured as a function of position of irradiation with a 100 μm step size. Figures 5a and b contain photocurrent maps spanning 2.0 by 1.5 mm^2 of the photoactive layer for representative devices without and with 4T-C_{60}, respectively. For ease of comparison, we normalized the recorded photocurrent by the maximum photocurrent in each device. With our color scheme, high current regions thus appear bright and low current regions appear dark. Bright-field optical images of the regions examined are shown as insets. The photocurrent map of the inverted solar cell without 4T-C_{60} in Figure 5a is highly nonuniform. We observe a bright spot corresponding to high current density levels; the photocurrents in the surrounding regions are very low in comparison. The lowest photocurrent recorded was only 4% of the maximum photocurrent. Comparing this photocurrent map against the bright-field optical image reveals that low photocurrent correlates with the presence of PCBM dendrites while high photocurrent stems from regions absent of dendrites, suggesting that these P3HT-rich regions must still contain PCBM in order for exciton dissociation and charge collection to occur. Indeed, acquisition of the elemental distribution via EDX in these nondendritic regions reveal evidence of oxygen and a carbon to sulfur ratio that is higher than that of P3HT alone, confirming the presence of some PCBM in the continuous phase. On the other hand, the photocurrent map obtained on the device whose photoactive layer incorporates 5 wt % 4T-C_{60} in

(55) Kim, J. B.; Lee, S.; Toney, M. F.; Chen, Z.; Facchetti, A.; Kim, Y. S.; Loo, Y. -L. *Chem. Mater.* **2010**, *22*, 4931.

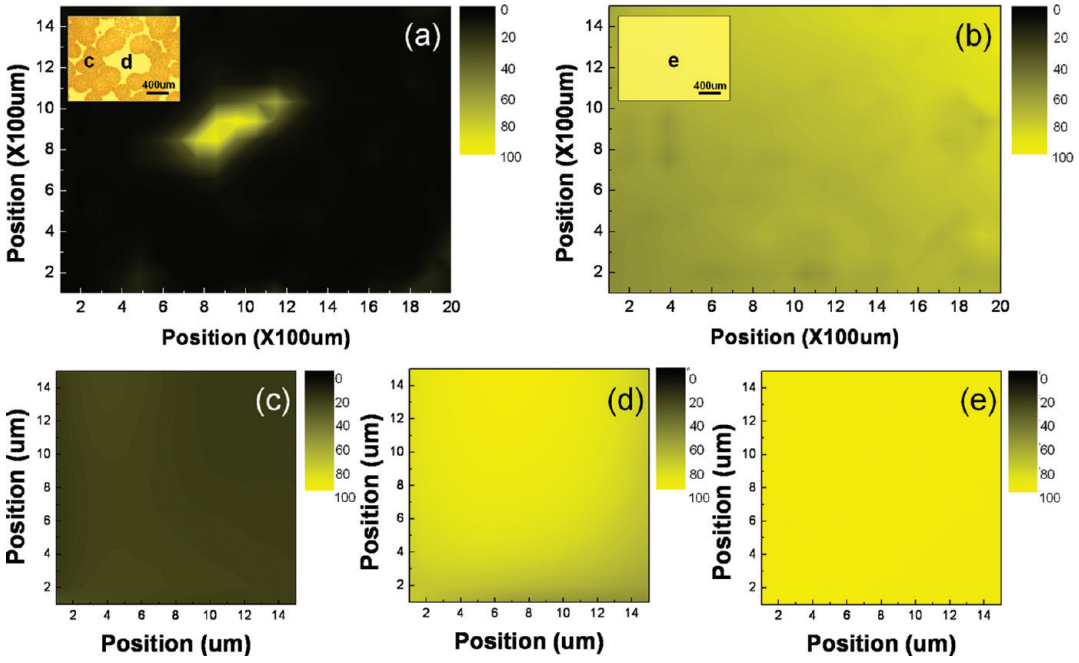

Figure 5. Spatially-resolved photocurrent maps of (a) an uncompatibilized, reference P3HT:PCBM solar cell and (b) one with 5 wt % 4T-C_{60}. Excitation was carried out with a 488 nm laser having a 1 μm spot size. The scanning area was 2.0 mm × 1.5 mm, data was collected every 100 μm. High-resolution scans of (c) the dendritic regions and (d) the continuous phase of a reference P3HT:PCBM solar cell and that of (e) the compatibilized P3HT:PCBM device with 5 wt % 4T-C_{60}. In the high-resolution scans, the same laser setup was used and the step size was reduced to 1 μm. The scan area was 15 μm × 15 μm. Insets show OM images and scan regions have been indicated for clarity.

Figure 5b is significantly more uniform. Across the entire area examined, the lowest photocurrent recorded was 60% the maximum photocurrent. Given that the spot size of the laser is only 1 μm, we were able to use the same setup to conduct higher-resolution photocurrent mapping. For this set of experiments, we chose to examine an area that is 15 by 15 μm^2. The photocurrent was measured at 1 μm intervals as the laser was scanned across the sample. Figure 5c represents a high-resolution photocurrent map acquired in a region comprising dendritic PCBM structures. This region is highlighted in the bright-field image in the inset of Figure 5a. The photocurrent in Figure 5c is generally low and spans only 22−30% of the maximum photocurrent recorded during the acquisition of the photocurrent map presented in Figure 5a. Figure 5d contains the photocurrent map corresponding to the nondendritic region in the bright-field image in Figure 5a. In this case, the photocurrents are higher and span 53−100% of the maximum photocurrent recorded in Figure 5a. The high-resolution photocurrent map of the inverted solar cell having 5 wt % 4T-C_{60} is shown in Figure 5e. The photocurrents are significantly more uniform by comparison; photocurrent variations across the entire 15 by 15 μm^2 region spanned 98−100% of the maximum photocurrent recorded in Figure 5b.

Our photocurrent measurements suggest that the nondendritic regions in annealed P3HT:PCBM devices without 4T-C_{60} must comprise PCBM in addition to P3HT. Demixing of P3HT and PCBM in such regions must occur on a length scale finer than our probe resolution in this study and yet appropriate for exciton dissociation as we observe non-negligible currents. The incorporation of 4T-C_{60} eliminates dendrite formation and arrests phase separation at a finer length scale than is observable. As a consequence, we observe uniform and high photocurrents in the compatibilized thin films. Collectively, these observations implicate crystallization of PCBM to be the driving force for macroscopic phase separation in blends of P3HT and PCBM. In the absence of any interfacial agents, extended annealing induces crystallization and rapid growth of PCBM domains.

Because small-molecule dyads are not precedent as compatibilizers, we also assessed the effectiveness with which nT-C_{60} can compatibilize P3HT and PCBM as a function of the number of conjugated thiophenes. The other molecules designed for this study contain 2 (2T-C_{60}; see Scheme 1 for chemical structure) and 8 (8T-C_{60}) thiophene units. We fabricated and tested P3HT:PCBM inverted solar cells in which the photoactive layers comprised 5 wt % 2T-C_{60} as well as those comprising 5 wt % 8T-C_{60}. Here, we have kept the weight fraction of the compatibilizing agent constant. We have also carried out experiments in which the molar fraction of the compatibilizing agent was kept constant; the results are qualitatively similar to what is reported below. Comparison of structural and electrical characterization between these experiments provided elucidation of the effects of thiophene chain length on the derivative's ability to compatibilize P3HT and PCBM. Figure 6a plots the efficiency of P3HT:PCBM inverted solar cells in which the photoactive layers comprise nT-C_{60}. Five devices were tested for each derivative; the error bars in Figure 6a represent variations in device characteristics. We observe a systematic increase in device efficiency with increasing thiophene chain length of nT-C_{60} after the devices are thermally annealed for 1 min. This systematic increase in the

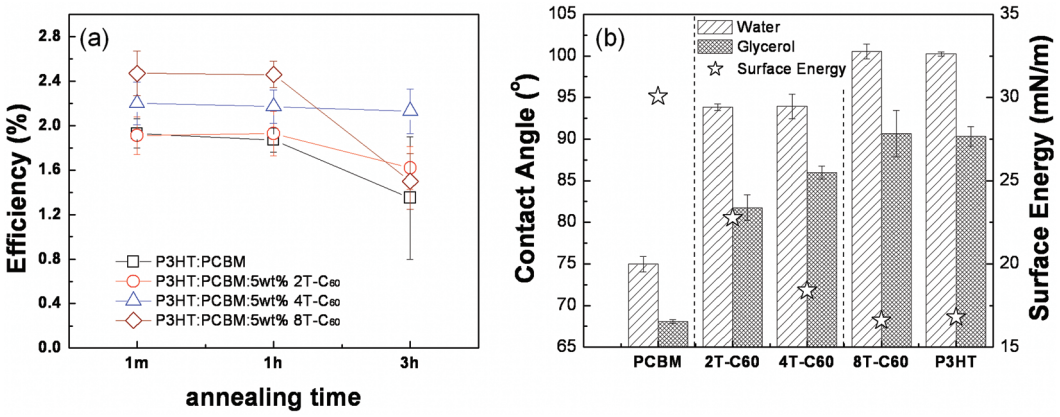

Figure 6. (a) Average efficiencies of P3HT:PCBM devices comprising 5 wt % 2T-C_{60}, 4T-C_{60}, and 8T-C_{60}. All devices were annealed at 170 °C under N_2 atmosphere. (b) Contact angles and surface energies of P3HT, nT-C_{60}, and PCBM.

average efficiencies can be attributed to increased light absorption of the active layers with the incorporation of dyads having increasing thiophene chain length.[56] While the addition of 4T-C_{60} reduces the interfacial energy between P3HT and PCBM, as evidenced by the constancy of the efficiency with extended thermal annealing, we observe that the addition of both 2T-C_{60} and 8T-C_{60} are less successful at stabilizing the device characteristics on extended thermal annealing. Of 5 devices tested, the average efficiency of P3HT:PCBM devices with 2T-C_{60} was 1.91 ± 0.17% with 1 min of thermal annealing at 170 °C. After thermal annealing at 170 °C for 3 h, the average efficiency decreased to 1.62 ± 0.19%. The 5 devices with 8T-C_{60} showed an initial average efficiency of 2.47 ± 0.20% with 1 min of thermal annealing at 170 °C; this quantity was reduced to 1.50 ± 0.25% after 3 h of thermal annealing. Structural characterization analogous to those carried out for 4T-C_{60} indicates that this reduction in device efficiency correlates with significant PCBM domain coarsening that takes place on thermal annealing. To understand why 4T-C_{60} is the most effective compatibilizer of those tested, we carried out contact angle measurements of neat films of 2T-C_{60}, 4T-C_{60}, and 8T-C_{60} as well as those of P3HT and PCBM to extract their surface energies. Static water and glycerol contact angles measured on these films are summarized in Figure 6b. From these contact angles, we estimated the surface energies of these species using the Owens and Wendt method;[40] these are also tabulated for completeness (Table 1). P3HT and PCBM have surface energies of 16.8 and 30.1 mN/m, respectively. We observe that 2T-C_{60} and 4T-C_{60} have surface energies of 22.8 and 18.4 mN/m, respectively. 8T-C_{60}, on the other hand, has a surface energy that is comparable to that of P3HT (16.6 mN/m). Furthermore, the volume fraction of thiophene in 8T-C_{60} is estimated to be 0.75 on the basis of published densities of poly-

Table 1. Contact Angle of Water and Glycerol on P3HT, nT-C_{60}, and PCBM Films, from which Surface Energies are Estimated

	water (deg)	glycerol (deg)	surface energy (mN/m)
PCBM	74.98 ± 0.90	68.08 ± 0.24	30.07
2T-C_{60}	93.84 ± 0.38	81.79 ± 1.52	22.75
4T-C_{60}	93.93 ± 1.48	85.99 ± 0.79	18.40
8T-C_{60}	100.52 ± 0.91	90.68 ± 2.80	16.60
P3HT	100.22 ± 0.26	90.32 ± 1.20	16.81

(3-dodecyl thiophene) and C_{60} (1.07 and 1.65 g/cm^3, respectively).[57,58] Given the asymmetry in volume fraction and the comparable surface energy of 8T-C_{60} and P3HT, 8T-C_{60} is likely to be miscible with P3HT. It is thus not surprising that 8T-C_{60} is ineffective at compatibilizing P3HT and PCBM. In the case of 2T-C_{60}, the thiophene segment is too short. Although the compound is still likely to reside at the interface between P3HT and PCBM (its surface energy is between those of P3HT and PCBM), it cannot effectively increase interfacial adhesion and arrest domain coarsening. PCBM dendrites are therefore observed on extensive annealing of photoactive layers comprising 2T-C_{60} as well. 4T-C_{60} possesses an intermediate surface energy and its thiophene segment is sufficiently long; its addition to P3HT and PCBM simultaneously reduces interfacial energy and increases interfacial adhesion. It is thus the combination of these characteristics that makes 4T-C_{60} the most effective interfacial agent of the three candidates we tested.

4. Conclusions

Exploiting the principles of classical polymer physics, we demonstrated 4T-C_{60} to be an effective interfacial agent for compatibilizing blends of P3HT and PCBM in thin films for organic solar cell application. Its incorporation reduces the interfacial energy between P3HT and PCBM and prevents significant domain coarsening on thermal annealing. The effectiveness with which the interfacial agent compatibilizes P3HT and PCBM is also sensitive to its architecture and molecular characteristics. Proper design of the interfacial agent can effectively arrest domain coarsening and prevent macrophase separation within photoactive layers of

(56) Colditz, R.; Grebner, D.; Helbig, M.; Rentsch, S. *Chem. Phys.* **1995**, *201*, 309.
(57) Tashiro, K.; Ono, K.; Minagawa, Y.; Kobayashi, M.; Kawai, T.; Yoshino, K. *J. Polym. Sci., Part B* **1991**, *29*, 1223.
(58) Swinnen, A.; Haeldermans, I.; vande Ven, M.; D'Haen, J.; Vanhoyland, G.; Aresu, S.; D'Olieslaeger, M.; Manca, J. *Adv. Funct. Mater.* **2006**, *16*, 760.

polymer solar cells, leading to robust and constant device characteristics.

Acknowledgment. This work was supported by the Photovoltaics Program at ONR (N00014-08-1-1175) and a Sloan Research Fellowship to Y.L.L.. Partial funding of an NSF-sponsored MRSEC through the Princeton Center for Complex Materials (DMR-081960) is also acknowledged. S.J.O. and C.R.K. acknowledge the support of the NSF CBET program (CBET-0854226). K.A. and C.N. acknowledge support from the Office of Naval Research under Award Numbers N00014-09-01-0250 and N00014-09-1-1117, and the Center for Re-Defining Photovoltaic Efficiency through Molecule Scale Control, an Energy Frontier Research Center funded by the U.S. Department of Energy, Office of Science, Office of Basic Energy Sciences, under Award DE-SC0001085. Portions of this research were carried out at the Stanford Synchrotron Radiation Lightsource user facility operated by Stanford University on behalf of the U.S. Department Energy, Office of Basic Energy Sciences. We also gratefully acknowledge Brad Olsen and Shong Yin for providing Igor routines and codes for GIXD data reduction.